
This manuscript has been submitted for publication in EARTH AND PLANETARY SCIENCE LETTERS. Please note that, despite having undergone peer-review, the manuscript has yet to be formally accepted for publication. Subsequent versions of this manuscript may have slightly different content. If accepted, the final version of this manuscript will be available via the 'Peer-reviewed Publication DOI' link on the right-hand side of this webpage.

Please feel free to contact any of the authors; we welcome feedback.

The large-scale troughs on Asteroid 4 Vesta are opening-mode fractures

Hui Ching Jupiter Cheng¹ and Christian Klimczak¹

¹Structural Geology and Geomechanics Group, Department of Geology, University of Georgia, Athens, GA 30602, USA

Keywords: planetary tectonics, Vesta, normal faulting, opening-mode fracture

Abstract

The Dawn mission at Asteroid 4 Vesta revealed two sets of enormous linear structures. Both sets are troughs—linear, negative-relief landforms—with one spanning around two-thirds of the equator and the other set located in the northern hemisphere. Previous work evaluated the shapes of the troughs and interpreted them to be analogous to grabens, which are landforms caused by faulting; however, an origin from opening-mode fracture origin was heretofore not considered. To distinguish between those origins, we investigate the map patterns, cross-sectional geometries, and variations of relief and width along the length of these troughs. Both relief and width are meaningful measurands that directly relate to the vertical displacement of faults or aperture of opening-mode fractures, respectively, and thus their variations along the structures may reveal differences in fracturing behavior. We map all major troughs on Vesta, including four equatorial and two northern troughs, and no map patterns diagnostic for faulting were identified. The troughs are bounded by scalloped rims and mainly show V- and bowl shapes in cross-section. Assessment of the variation of reliefs of the two opposing trough-bounding scarps reveals that the relief maxima for each of the investigated troughs are located off-center and at different locations along the trough they bound. In contrast, we find that both the individual and cumulative variations in trough width have their maxima near the center of the trough. These map patterns and

geomorphologic characteristics are largely inconsistent with the mechanics of graben formation but instead point to an opening-mode fracture origin. In addition, our calculations of lithospheric strength evolution and predicted fracturing behavior reveal that Vesta's lithosphere has been dominated by a thick brittle portion throughout its history. Solutions to the Coulomb criterion considering a range of strengths properties of intact to fractured basaltic materials are in support of jointing as the major fracturing mode in at least the upper ~14 km of Vesta's lithosphere.

1. Introduction

1.1. Vesta's tectonics

The Dawn mission (Russell and Raymond, 2011) explored Asteroid 4 Vesta, from hereon referred to as Vesta, and revealed the presence of two sets of large-scale linear structure. The equatorial troughs are varying in width from several 100s of meters up to about 20.5 km, bounded by steep scarps, and encircling about two-thirds of the asteroid with its largest one named Divalia Fossa. The northern troughs are oriented northwest-southeast showing a difference in orientation from the equatorial troughs of approximately 30°. They are exposed only in the northern hemisphere with their southern extent truncated by the equatorial troughs. The largest of the northern troughs is named Saturnalia Fossa. The photomosaics and digital terrain model derived from Dawn Framing Camera (FC) images (Sierks et al., 2011) allow for detailed mapping and structural analysis of these troughs. Previous analysis shows that poles of vertical planes defined along the two sets of troughs cluster near the center of Veneneia and Rheasilvia impact basins that are located in the south polar region. This relationship was interpreted as a genetic link between the two impacts and sets of troughs (Jaumann et al., 2012).

Divalia Fossa, the most prominent of the equatorial troughs, was observed to be flat-floored and interpreted as a graben, formed by normal faulting, with vertical displacements in excess of 5 km (Buczowski et al. 2012). Subsequently, multiple studies have interpreted Divalia Fossa and similar troughs on Vesta as grabens, half-grabens, and horst-graben structures (Ruesch et al., 2014; Schäfer et al., 2014; Scully et al., 2014; Yingst et al., 2014). Several modeling works have been conducted to determine the specific tectonic causes for the faulting, including numerical modeling to simulate the amount of deformation associated with the formation of the Rheasilvia basin (Bowling et al., 2013), and combining laboratory and numerical experiments to model subsurface failure as a consequence of oblique impacts into a spherical target (Stickle et al., 2015). However, the rheology and brittle strength of Vesta's lithosphere have not been evaluated, and other fractures types have not been considered to partake in the tectonics of the asteroid. In particular, opening-mode fracturing, such as jointing, is a ubiquitous fracturing behavior in the upper portion of the Earth's lithosphere, and it remains to be assessed in how far it played a role in the formation of the troughs.

1.2. Normal faulting vs. Jointing

Brittle failure under an extensional tectonic regime, where the overburden pressure represents the maximum principal stress, occurs through the formation or slip on joints and normal faults. Jointing and normal faulting are different in terms of their mechanics, the stresses needed to form them, map patterns, cross-sectional geometries, and kinematics.

Joints are planar discontinuities in a rock where the fracture walls move perpendicularly apart from one another forming opening displacement (Pollard and Aydin, 1988), and thus they are considered opening-mode fractures along with veins and dikes. In contrast, faulting shows

movement parallel to the fault plane, which is referred to as sliding-, or tearing-mode fracturing. In particular, normal fault displacement is achieved by frictional sliding when the hanging wall, the rock mass above the fault plane, slips down relative to the footwall, the rock mass beneath the fault plane. Joints form when tensile stresses reach the tensile strength of the rock in a direction largely perpendicular to the fracture plane. In contrast, normal faulting occurs by frictional sliding that occurs only when all principal stress components are compressive, the maximum stress is oriented vertically and equal to the overburden pressure and the minimum principal stress acting horizontally. In a lithosphere under extension, joints propagating from the surface to depth reach a critical depth, where they transition to become normal faults when the overburden is large enough to shift tensile stresses into the compressive regime, such as observed at the Almannagjá normal fault at the Þingvellir rift valley of southwest Iceland, which shows an opening displacement of 60 meters and vertical displacement of 40 meters (Gudmundsson, 1992, 2011).

Normal faults commonly appear as grabens, which are narrow, negative relief structures bounded by oppositely dipping normal faults, with dip directions toward one another, that create a down-dropped block in the center (Fossen, 2009; Schultz et al., 2007). Grabens display a wide range of map patterns, which some are diagnostic for normal faulting, and found on many different planetary bodies. They generally display straight to arcuate bounding scarps and are commonly segmented, showing en échelon patterns and transfer zones between overstepping segments, also referred to as relay ramps. Grabens may also involve multiple faulted borders and floors, which is an analog of complex terrestrial rift systems (Hauber and Kronberg, 2005). In some cases, pit crater chains, which are connected circular depressions that form by the collapse of material into subsurface voids, are found aligned with or superimposed within graben, such as in those documented in detail in Hawaii (Okubo and Martel., 1998) and on Mars (Wyrick et al., 2004). In

terms of displacement, their maxima are typically centrally located along the faults tapering to zero at the fault tips (e.g., Dawers et al., 1993). Displacements scale positively linear with fault length (Schultz et al., 2006). In cross-sectional view, grabens typically appear as a flat-floored depression, bounded by two (or more) scarps facing one another.

In contrast, joints can appear as a straight trace of continuous single crack or segmented and discontinuous en échelon traces of subparallel small segments in map view. Although joints can occur as isolated structures, they commonly occur as sets of parallel joints. Closely spaced joints may interact with each other forming hook-shaped linkages (Pollard and Aydin, 1988). Joints have their maximum displacement, commonly referred to as aperture, centrally located along the structure, which gently tapered at the two ends (Vermilye and Scholz, 1995), which, in the map view, appear as wide troughs that narrow toward the tips. Their maximum aperture scales positively sublinear with its length (Olson, 2003). In contrast to a graben, a vertical joint can be expected to show as a narrow V shape, but it can be degraded due to slope instability to appear as a wide bowl-, or V shape by secondary infilling of collapsed materials.

In this paper, we first investigate the map patterns, cross-sectional geometries, and shape variations of several large-scale troughs in detail to assess whether they are opening- or sliding-mode fractures. Based on the previously published interior constitution and thermal evolution models, we then derive strength-depth profiles to characterize the rheologic structure of Vesta's lithosphere and determine the predicted fracturing behavior in its brittle regime. Knowledge of how these large-scale structures are formed has implications for the tectonics and fracturing behavior for Vesta and other low-gravity planetary bodies.

2. Trough map patterns

We use Dawn FC images with a resolution of 60 m/pixel and the ~93 m/pixel digital terrain model (DTM) as a basis for structural mapping. The DTM is based on the shape model of Vesta derived from FC images with a lateral resolution of ~93 m/pixel and a vertical accuracy of about 6 m (Preusker et al., 2014). The two large sets of troughs and their related landforms, the bounding scarps and pit crater chains, are included in our mapping. For our structural mapping, we utilize ESRI's software ArcGIS to create hillshade images with different illumination conditions and draw topographic cross-sections at ~5 km intervals across the troughs. Trough-bounding scarps are defined where a sharp surface break is observed on the topographic profiles, which were then traced on the hillshade images. Structures identified as *certain troughs* are mapped where negative topography is bounded by two facing scarps. Long depressions with only a single bounding scarp are mapped as *inferred troughs*. Troughs of any category were grouped into one structure when multiple troughs were aligned but it was clear that they were only separated by one or several impact craters. Pit craters and chains thereof are included in our mapping, as they are aligned with the equatorial troughs (Buczkowski et al., 2012; Jaumann et al., 2012) and are frequently found in association with grabens on other planetary bodies (Wyrick et al., 2004). They are mapped where there is a series of at least three aligned circular to elliptical, steep-sided depressions that lack diagnostic features for impact craters or volcanic pits, including elevated rims, ejecta deposits, or lava flows.

Previous work mapped 86 equatorial and 7 northern trough lineaments (Jaumann et al., 2012; Yingst et al., 2014) but those works have not considered that some of the troughs are part of the same structures. Based on our mapping criteria, we identified a total of 55 individual trough lineaments comprised of 155 bounding scarps as well as 30 pit crater chains (Figure 1). The structural map is included as shapefile in the supplementary materials. Of the 55 structures, 36

trenches are classified as certain and 19 are inferred. But out of those, 30 certain and 9 inferred trenches form six main structures. We assigned each of them a number from south to north for further analysis and presentation. The equatorial set consists of closely spaced E–W striking trenches 1 to 4, with lengths of 335–815 km and widths up to 20.5 km. The most prominent trench (here trench 2) is named Divalia Fossa. Trench 1 consists of at least three segments separated far apart by long inferred trench lineaments, while trenches 2 to 4 consist of certain trenches lineaments superposed by few impact craters. Trenches 5 and 6 are part of the northern set of trenches. Trench 6 is named Saturnalia Fossa. Note that the southern extensions of these northern trenches are truncated by the equatorial set, therefore their true lengths are not preserved. All trenches described are mapped as being isolated, continuous, and subparallel among their own sets (Figure 1).

Map patterns diagnostic for faulting, such as en échelon segmentation, relay ramps, or multiple faulted borders and floors were not identified for any of the structures on Vesta. Instead, we find that, in all cases, trench-bounding scarps are scalloped (Figure 2a). In fact, the rims are too scalloped or too degraded to be interpreted as normal faults. In contrast, Matronalia Rupes and other scarps forming the rim of the Rheasilvia impact basin, which is proposed to be coeval to the equatorial trenches, appear remarkably fresh. Map patterns diagnostic for jointing, such as hook-shaped linkages and en échelon traces of subparallel openings, are also not readily apparent. Instead, we find that degradation and slope instability may have produced the current map characteristics of the trenches.

Consistent with previous studies (Buczowski et al., 2012; Jaumann et al., 2012), our mapped pit crater chains are found to be aligned with the equatorial trenches (Figure 1). Generally, pit crater chains are found to be located on the floors of planetary grabens (Wyrick et al., 2004), but on Vesta, none of them are found to occur within a trench, i.e., inbetween the two bounding

scarps. Pit crater chains on Vesta show a high variability of map patterns but their full number and extent are unclear due to the superposition of impact craters. Only trough 1 is observed to show a direct transition from trough into a pit crater chain (Figure 2a). This trough narrows and terminates in a pit crater chain, and smaller pits align with the trough further away from the termination of the trough. One completely preserved pit crater chain has larger pits in the middle and smaller pits at the two ends of the chain (Figure 2b). Following these map observations, the structures possibly represent multiple stages of trough formation where the scalloped edges of the troughs may be coalesced pits forming from collapsed openings and unstable slopes. That pits are getting larger towards the center of the chain is indicative of the opening-mode displacement profile of a joint. Therefore, the large-scale troughs could be coalesced pits that formed from collapsed joints.

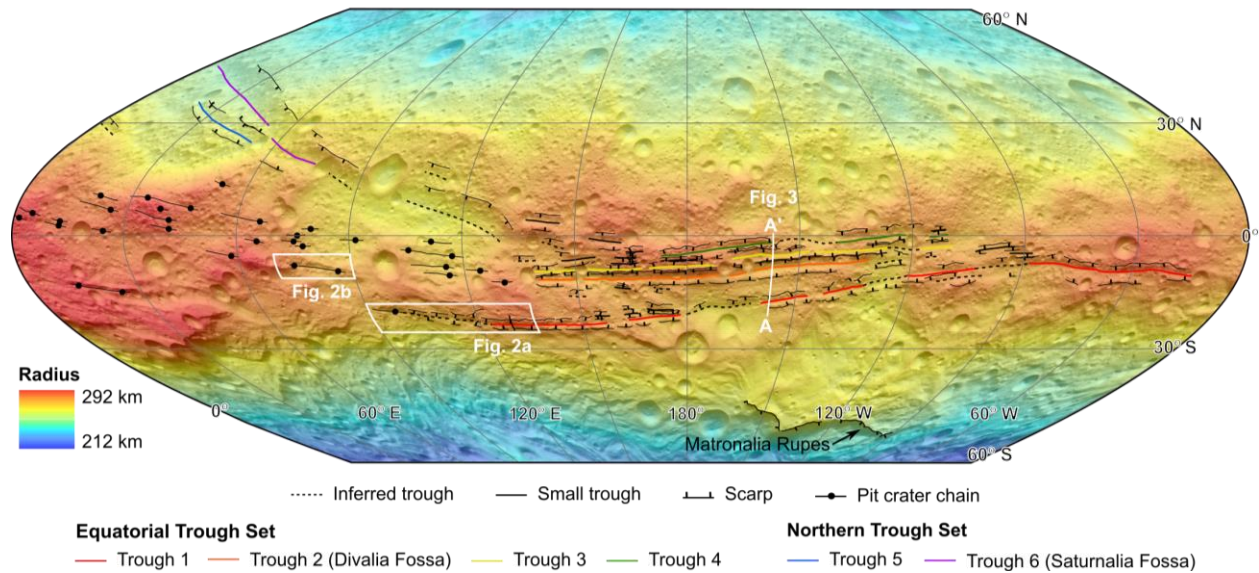


Figure 1. Digital terrain model of Vesta overlaid on hillshade showing a structural map of large-scale troughs and pit crater chains. The map is displayed in sinusoidal projection extending between latitudes 60°N to 60°S and longitudes 0° to 30°W. Refer to text for the definition of structural map units. Locations and geographic extents of subsequent maps and a topographic section are indicated by white boxes and a line, respectively. <2 columns, color>

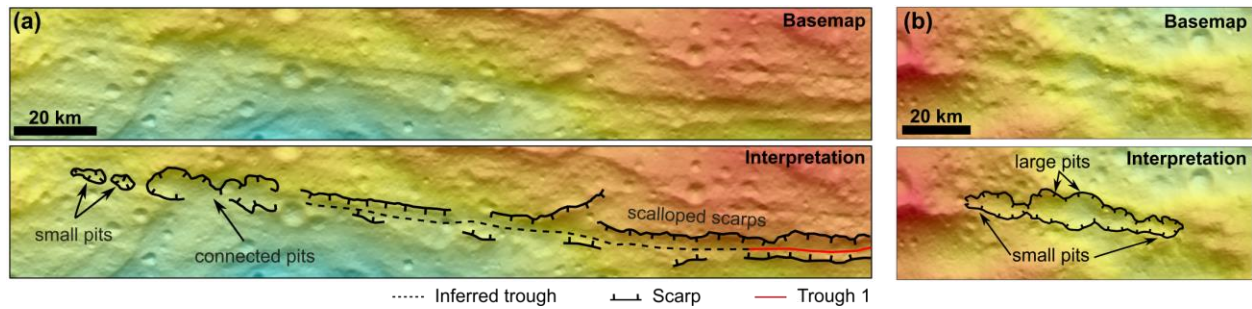


Figure 2. Basemap (top) and structural interpretations (bottom) of scalloped scarps and pits and pit crater chains. (a) Trough 1 terminates into coalesced pits also showing smaller pits aligned with and beyond the termination of the trough. (b) A pit crater chain with larger pits in the middle and smaller pits at the two ends. Refer to Figure 1 for the location on Vesta. <2 column, color>

3. Trough geomorphology

Previous work evaluated that the morphology of the troughs displays a classic flat-floored shape with both walls having a similar slope, which led to an interpretation for the structures to be analogous to grabens on other terrestrial planets (Buczowski et al., 2012). Based on that interpretation, Buczowski et al. (2012) measured at a handful of locations the topographic differences between the rim and floor of the Divalia and Saturnalia Fossæ and related them to the vertical displacement component of graben-bounding normal faults. To further examine the cross-sectional geometries of, and relief and width variations along the troughs, we extract and analyze 233 topographic profiles with evenly spaced at 5 km across six large troughs, respectively. The 233 individual profiles and measurement data are provided in the supplementary material.

3.1. Cross-sectional trough geometries

Cross-sectional shapes for the six troughs were assessed along our 233 extracted profiles. Note that the majority of profiles contain more than one trough so that a total of 392 individual trough geometries were analyzed. All profiles were visually analyzed for topographic changes

between the trough rims to identify whether or not the cross-sectional trough geometry is flat-floored, i.e., no major topographic changes in the center of the trough, or whether a different geometry is observed. Trough geometries that lack distinctive rims or are superposed by impact craters are classified as inconclusive. One representative profile of the equatorial set is shown in Figure 3, which shows four troughs with troughs 1, 2, and 3 displaying a clear bowl shape, and trough 4 having a V-shape. Among all assessed topographic profiles, 207 out of 260 conclusive troughs display either V- or bowl-shaped geometries and only 53 flat-floored shapes are observed. These findings show that the vast majority of troughs do not show the cross-sectional geomorphology that is typical for graben.

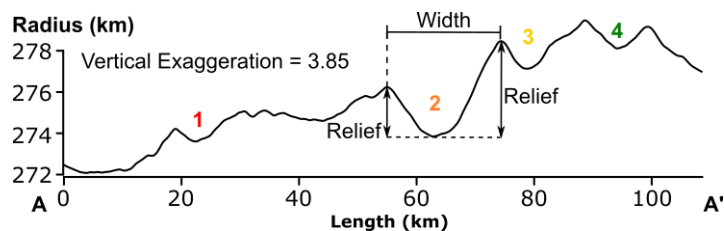


Figure 3. Typical topographic expression of troughs on Vesta. A topographic profile A–A’ showing the geometry of four major equatorial troughs. The trough width and relief of two rims are labeled for trough 2. Note that the trough shapes are not flat-floored, but instead bowl- and V-shaped. <1 column, color>

3.2. Shape variations along troughs

3.2.1. Trough reliefs

Buczowski et al. (2012) analyzed the topographic differences between the trough floor and rim of Divalia and Saturnalia Fossæ and related them to the vertical displacements of faults forming graben. We expand upon this analysis by assessing a total of six troughs also including

Divalia and Saturnalia Fossæ but with a denser sampling of the topographic data (Supplementary material). Structural reliefs for the trough-bounding scarps for each major trough are assessed in 5 km intervals. The shortest trough, trough 5, was measured to be 115 km long and includes 24 measurements, whereas the longest trough, trough 1, with a length of 835 km, has 168 measurements per trough-bounding scarp. The reliefs of scarps are determined by the maximum elevation differences between the trough floor and rims, as indicated in Figure 3. The measured values are plotted along the normalized length of map trace for comparison of maximum reliefs of the two trough-bounding scarps to one another and with respect to the center of the trough length (Figure 4). A graben origin predicts the vertical displacements of the bounding faults, represented here by scarp reliefs, to have their maxima located centrally along the length of the trough and taper to zero toward the tips. The two profiles per trough, one for each of the trough-bounding scarp, are expected to mimic each other, considering that no fault segmentation and linkages are observed. As the southern portion of the northern troughs is no longer preserved, their true maxima and location along the trough cannot be determined, nonetheless, we analyze them to investigate if part of the relief distribution profile shows characteristics typical for faults.

Figure 4 displays two relief distributions for each of the six troughs. Trough 1 is separated into three segments by long muted troughs far from each other, which makes it difficult to determine if they belong to a single or multiple structures; the maximum reliefs are marked for each of its segments. In total, the length of trough 1 is 835km, and its maximum reliefs of the northern and southern rims are 4.74 km and 2.78 km, respectively. Trough 2, Divalia Fossa, is 400 km long with the maximum reliefs of 5.73 km on the northern rim and 2.96 km on the southern rim. Its northern rim has a large relief among the equatorial set, consistent with the finding by Buczkowski et al. (2012). Trough 3 is 495 km long with the maximum reliefs of 2.92 km and 2.82

km on the northern and southern rims, respectively. Trough 4 is 345 km long with the maximum reliefs of 3.22 km and 2.68 km on the northern and southern rims, respectively. Among the 8 distributions of the equatorial set, only the southern rim of trough 3 displays a peaked relief distribution with a maximum relief near the center along the length of the trough and tapering toward the tips (Figure 4a), whereas the other 7 profiles show maximum reliefs located off-center or displaying multiple peaks. Our results for Divalia Fossa are also consistent with the relief distribution presented in Buczkowski et al. (2012). In addition, we note that none of the four equatorial troughs show symmetrical shapes with relief distributions of the two trough-bounding scarps mimicking each other (Figure 4a).

For the northern set, the traceable length of trough 5 is 115 km with the maxima of 1.29 km and 3.99 km on the two scarps, whereas the traceable length of trough 6 is 275 km and its maxima of structural relief are 4.2 km and 6.89 km. Similar to those on the equatorial trough sets, the two maxima pairs of the northern troughs are not found at the same location along their relief distribution profile (Figure 4b).

In summary, only one out of 12 relief distributions shows a maximum in their center. In addition, none of the troughs have relief distributions where both trough-bounding scarps have similar shapes, making the troughs highly asymmetric in cross section. These findings are atypical for normal faulting and thus cannot be considered in support of these landforms to be grabens.

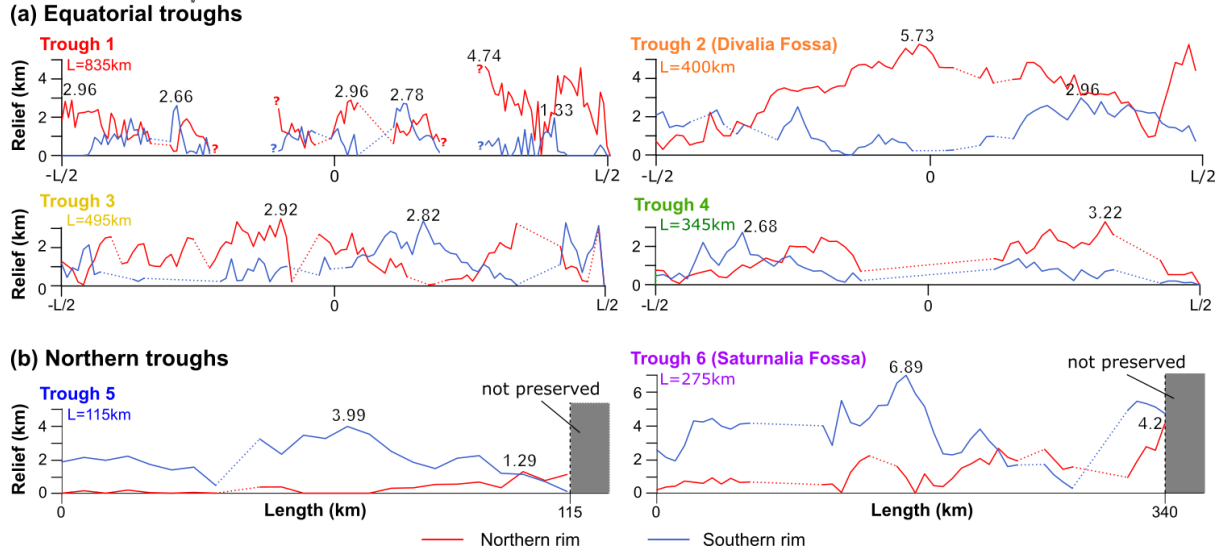


Figure 4. Relief distributions of all analyzed troughs. The reliefs of (a) equatorial set are plotted along the location of the trough normalized over total trough length, L . The numerical values of maxima (in km) are labeled at their locations long the trace. Scarps bounding troughs on the north are plotted in red, and southern scarps are plotted in blue. Note that the true extent of the northern troughs (b) is not preserved and thus total length and maximum relief are unknown, which the reliefs are plotted against the traceable length in km. <2 columns, color>

3.2.2. Trough widths

As with faults, opening-mode fractures also typically have displacement distribution profiles that display centrally located maxima that taper to zero at the fracture tips. But as the mode of displacement differs, where the opening, or aperture, is formed perpendicular to the fracture surface, such displacement must be investigated on Vesta by studying the trough widths. Trough widths are defined by the horizontal distance between the elevated portions of the two trough-bounding scarps measured perpendicular across the trough, as shown in Figure 3. We extract width measurements from the previously extracted topographic sections (supplementary material) across each of the previously analyzed troughs and also plot them along the length of the trough set from

west to east (Figure 5). The distributions are then analyzed for the location of maxima. These individual profiles are also added up to identify the cumulative widths for each of the two trough sets to explore their potential total opening-mode displacement.

Our width distribution results are shown in Figures 5a and b for the equatorial trough set. As with our relief analysis, trough 1 (Figure 5a) has three segments, and it is difficult to determine if it is a single or multiple structures. We have marked the maximum reliefs for each of its segments. The profile indicates that there is a general widening of trough 1 toward the east with the widest measurement of 20.4 km occurring near the easternmost tip. Troughs 2, 3, and 4 have maximum widths of 20.5 km, 15.8 km, and 17.3 km, respectively. Divalia Fossa (trough 2) is the widest trough of the equatorial set. The width maxima of troughs 2 to 4 all occur at a similar longitudinal position on Vesta, which is also centrally located along the length extent of the trough set (Figure 5a). These maxima are all skewed toward the east. The cumulative width distribution of the equatorial trough set shows a ~800 km long profile with one general maximum of 60.8 km at the center of the overall length trace, tapering toward the tips (Figure 5b).

The individual and cumulative width distributions of northern troughs are presented in Figure 5c and d. As an unknown portion of the southern extent of this trough set is not preserved, the full extent of their width distribution cannot be determined. However, the preserved portions show that trough 5 and 6 have a maximum width of 18.9 and 42 km, respectively. Saturnalia Fossa (trough 6) is the widest trough of the northern set. The relative location of their maxima along their full length and profile skewness are undetermined. The cumulative width distribution of the northern trough set shows a ~280 km long profile with one maximum of 56.2 km at around 110 km, tapering towards the western end while the eastern end is not preserved. The systematic changes and shapes of both the individual and cumulative profiles for both trough sets are

consistent with the mechanics of opening-mode fractures and we thus consider them as support of an opening-mode fracture origin.

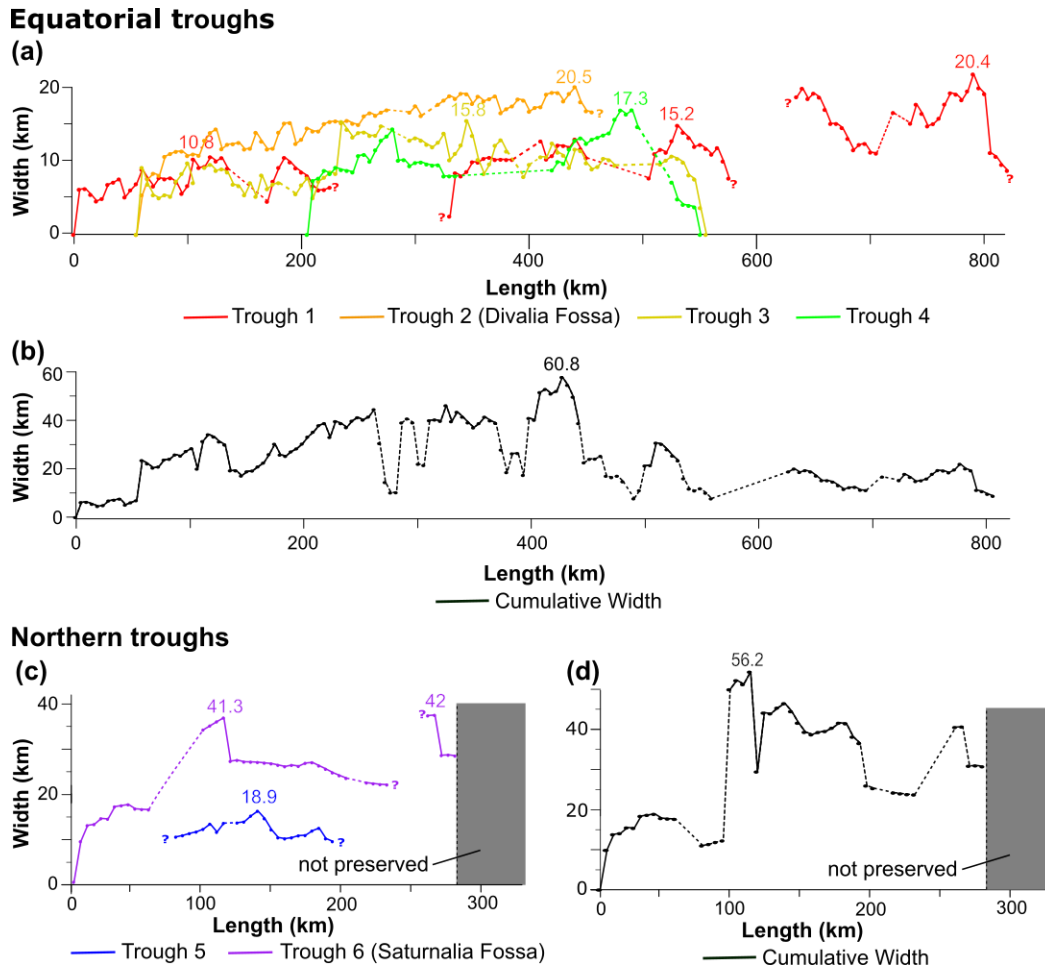


Figure 5. Width distributions of all analyzed troughs. (a) Individual and (b) cumulative width profiles of the equatorial set of troughs 1 to 4. (c) Individual and (d) cumulative width profiles of the northern set of trough 5 and 6. The numeric values of width maxima are labeled (in km) at their locations long the trace. Note that the true extent of the northern troughs (b) is not preserved and thus the true length and maximum width are unknown. <1.5 column, color>

4. Lithospheric strength and fracturing behavior

Next, we derive strength-depth profiles to characterize the rheologic structure of Vesta's lithosphere and determine the predicted fracturing behavior in its brittle regime. On a low-gravity body, such as Vesta, the thickness of the total lithosphere, the gravitational acceleration-dependent lithostatic pressure-depth function, and the transition from brittle to ductile behavior are all important factors that need to be accounted for when assessing large fractures. Thus, the first step is to derive the gravitational acceleration profile for Vesta based on previously published interior constitutions. Vesta is a differentiated asteroid, and previous studies assessed the thicknesses, compositions, and densities of core, mantle, and crust using geophysical and spectral data from the Dawn mission and howardite-eucrite-diogenite (HED) meteorites, for which Vesta is widely believed to be the parent body. Vesta is found to have an iron core with a diameter of ~108 km and density of ~7850 kg m⁻³ (Ermakov et al., 2014; Russell et al., 2012; Ruzicka et al., 1997), a ~118 km thick (Ermakov et al., 2014) olivine-rich mantle with the density of ~3400 kg m⁻³ (Russell et al., 2012; Ruzicka et al., 1997; Zuber et al., 2011), and a ~36 km thick basaltic crust with the density of 2900 kg m⁻³ (Russell et al., 2012; Ruzicka et al., 1997; Zuber et al., 2011). Using such 3-layer interior structure model (Figure 6a), we calculate the gravity acceleration profile of Vesta using:

$$\frac{\delta g}{\delta r} = 4\pi G \rho_r r - 2 \frac{g}{r}, \quad (1)$$

where g is gravitational acceleration, r is the radius of the body, G is the gravitational constant, and ρ_r is local material density. Our calculated surface gravitational acceleration is 0.26 m/s² (Figure 6b), which is consistent with the values measured by the Dawn spacecraft, ranging from 0.23 to 0.27 m/s² (Ermakov et al., 2014). The acceleration due to gravity gradually decreases with depth to the lower mantle at ~120 km, where it increases until it reaches the core-mantle boundary.

The gravity acceleration then drops linearly to zero at the center of the core (Figure 6b). The result is consistent with the calculation by Stickle et al. (2015).

Next, we utilize our calculated gravity acceleration profile to assess how overburden pressure, P , changes with depth, as given by:

$$\frac{\delta P}{\delta r} = -\rho_r r g. \quad (2)$$

The resulting pressure profile is shown in Figure 6c. Overburden pressures increase with depth in a roughly linear fashion from 0 MPa at the surface to ~120 MPa at the core-mantle boundary and then increase more rapidly in the core.

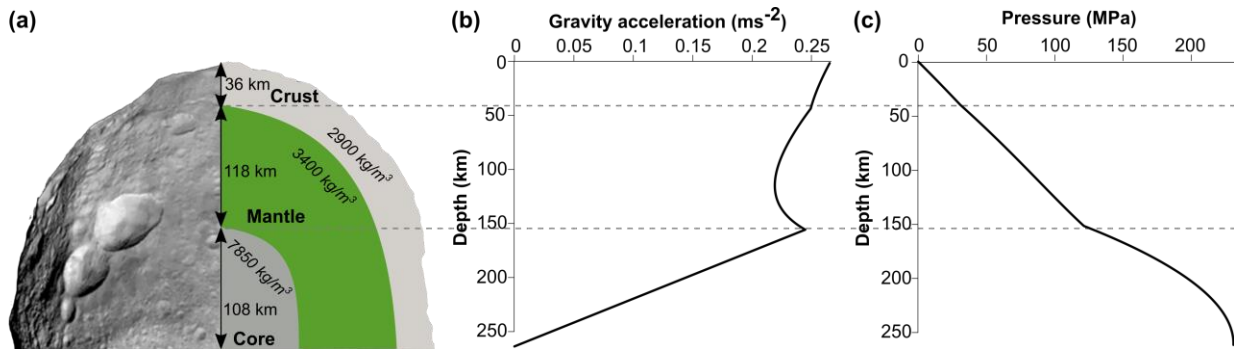


Figure 6. (a) A three layer-model of Vesta's interior was used to inform gravitational acceleration-, and pressure-depth profiles. (b) Gravitational acceleration-depth profile. (c) Pressure-depth profile. Dashed lines across the three diagrams indicate crust-mantle and mantle-core boundaries. <2 columns, color>

The overburden pressure plays an important role in defining lithospheric strength. Lithospheres are controlled by both brittle and ductile properties of its constitutive rock, and its strength is determined by the weakest rheology at a certain depth for a given stress. The upper portion of a solid surface body with low temperature and confining pressure is controlled by brittle behavior (Byerlee, 1978) with the yield stress increasing linearly with depth, independent of the

rock type and surface condition (Byerlee, 1978). Note that we follow the geologic sign convention in our calculations, where tensile stresses are negative and compressive stresses are positive. The rock strength can be determined by the equations:

$$\frac{\sigma_1}{\sigma_3} = \frac{S_v}{S_h} = (\sqrt{\mu^2 + 1} + \mu)^2 \text{ for extension} \quad (3)$$

and

$$\frac{\sigma_1}{\sigma_3} = \frac{S_H}{S_v} = (\sqrt{\mu^2 + 1} + \mu)^2 \text{ for shortening,} \quad (4)$$

assuming that P in Equation (2) corresponds to either the maximum (σ_1) or minimum (σ_3) principal stress component with zero pore fluid pressure, where S_v is the vertical stress, S_h and S_H are the minimum and maximum horizontal stresses, respectively. The coefficient of friction, μ , is a measure of the amount of friction existing between two sliding surfaces, which can be determined by analyses of the orientation of surfaces along which gravity sliding takes place on natural rock surfaces. We consider a value of $\mu = 0.6$ for both crust and mantle, which is a good representation of rock regardless of the rock type (Byerlee, 1978).

In the lower portions of the lithosphere, where temperatures are higher, ductile behavior dominates by several microstructural deformation mechanisms, which are combined under the term *creep*. Here, the strength sharply decreases with increasing temperature and is defined by a thermally activated power law (Burov and Diament, 1992; Mackwell et al., 1990; Ranalli and Murphy, 1987):

$$(\sigma_1 - \sigma_3)_d = \sqrt{\frac{n}{A}} \dot{\epsilon} \exp\left(\frac{Q}{nRT}\right), \quad (5)$$

where $\dot{\epsilon}$ is the strain rate, A and n are material constants, Q is the activation energy of creep, R is the gas constant ($8.31447 \text{ J mol}^{-1} \text{ K}^{-1}$), T is temperature. For our calculations we consider strain rates bracketed by 10^{-14} and 10^{-20} s^{-1} . The faster strain rate of 10^{-14} s^{-1} represents active deformation, such as found at orogenic belts (Pfiffner and Ramsay, 1982), whereas the slower strain rate of 10^{-20} s^{-1} is representative of deformation found on one-plate, stagnant lid bodies, such as Mercury (Crane and Klimczak, 2017), which is one to two orders of magnitude slower than that found at intra-plate continental tectonic settings (Gordon, 1998). For creep parameters, we take the widely-used properties of Maryland diabase ($n = 3$, $A = 6.3 \times 10^{-2} \text{ MPa}^{-n} \text{ s}^{-1}$, $Q = 276 \text{ kJ mol}^{-1}$) for the crust (Caristan, 1982), and dry olivine ($n = 3$, $A = 1 \times 10^4 \text{ MPa}^{-n} \text{ s}^{-1}$, $Q = 510 \text{ kJ mol}^{-1}$) for the mantle (Goetze and Evans, 1979). We utilize the simulated thermal evolution from Fu et al. (2014), which considered three time steps for each of their two end-member models; one with no megaregolith and the other with a 5-km-thick megaregolith layer.

Results for possible lithospheric structures of Vesta are shown in Figure 7 for the end-member cases of no megaregolith (top row) and with megaregolith layer (bottom row) at different times in Vesta's thermal evolution (Fu et al., 2014). The ages refer to time after the cessation of convection, which has been estimated to be short ($<10 \text{ Ma}$) after asteroid accretion (Sternborg and Crowley, 2013). All strength envelopes are plotted for the crust and mantle with a total thickness of 154 km. Lithospheric strength in the core is not calculated as there are too many unknowns of the thermal structure and material properties there. Any brittle behavior in the core, if present, especially with present thermal conditions, should mimic the shape of the curve of the overburden pressure profile (Figure 6c).

Our results of Vesta's lithospheric structure indicate that the crust and upper mantle down to $\sim 100 \text{ km}$ are entirely brittle for every combination of our parameter space, while the lower

mantle is only in the ductile regime early in Vesta's history and for the lower bracket of considered strain rates.

In particular, for the case without megaregolith, the brittle-ductile transition (BDT) occurs at a depth of ~ 100 km at 20–100 Ma (Figure 7a). At 500 Ma, the BDT migrated deeper to ~ 110 km and ~ 135 km with a lower and higher strain rate, respectively (Figure 7b). At present, both crust and mantle are completely brittle for our considered strain rates (Figure 7c). For the case with megaregolith, this 5-km-thick layer slows the cooling process of the asteroid by its low thermal conductivity. In Vesta's early history, the strength envelopes with insulating megaregolith layer (Figure 7d) is nearly indistinguishable from the one without regolith (Figure 7a), but the lower mantle remains in the ductile regime for much longer, potentially until 1500 Myr after accretion for the slow strain rates, while the crust and mantle would have been entirely brittle for fast strain rates at that point in time (Figure 7e). Crust and mantle are brittle for both strain rates at present (Figure 7f).

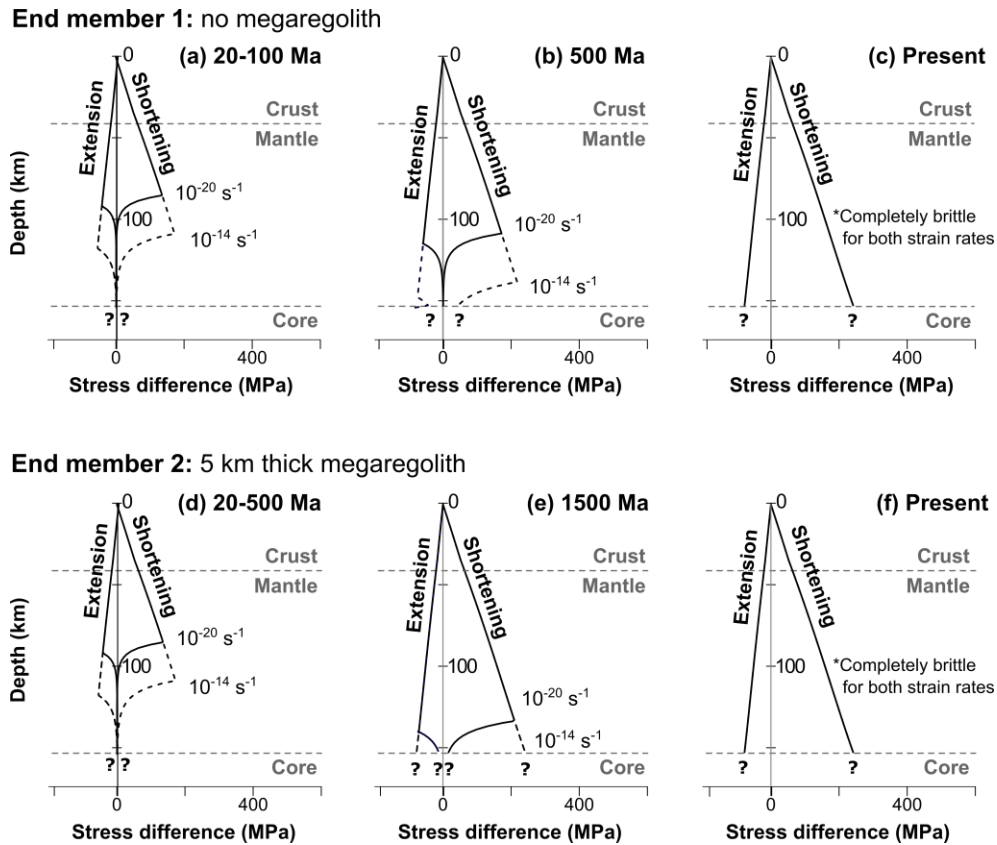


Figure 7. Strength envelopes and evolution for lithospheres under extension and shortening calculated for scenarios where Vesta has no megaregolith (top row) or with 5 km thick megaregolith (bottom row). Lithospheric structures with no megaregolith at (a) 20–100 Ma, (b) 500 Ma, and (c) present. Lithospheric structures with insulating megaregolith at (d) 20–500 Myr, (e) 1500 Myr, and (f) present. The time steps and end-members are based on the thermal evolution simulated by Fu et al. (2014). <1.5 column, black and white>

Our results establish that Vesta’s lithosphere is thick and that the crust and much of the mantle were in the brittle regime throughout Vesta’s history for every combination of plausible parameters. The deformation behavior in the lithosphere can thus be further assessed with a brittle failure criterion. We employ the Coulomb criterion to assess the stress magnitudes needed for overcoming the resistance to frictional sliding of two fracture surfaces in contact to produce faults. For tectonics on Vesta, we find the Coulomb criterion most suitable, because of its simplicity,

relying on only few assumptions, but allowing to include the universally applicable cohesive and frictional properties of rock. The principal stress form of the Coulomb criterion, which allows studying faulting as a function of depth, is given by:

$$\sigma_1 = \sigma_c + \sigma_3(\sqrt{\mu^2 + 1} + \mu)^2, \quad (6)$$

where σ_c refers to the unconfined compressive strength. The range of values for the uniaxial compressive strength of intact basalt is 266 ± 98 MPa (Schultz, 1995). We explore the σ_c of 168 MPa, 233 MPa and 364 MPa to capture the full range of unconfined compressive strength values of intact basalt. Again, we consider a value of $\mu = 0.6$ for both crust and mantle regardless of the rock type (Byerlee, 1978). For extensional tectonic regimes, the overburden pressure, P , acts vertically as the maximum principal stress, σ_1 . We substitute our overburden pressure profile (Figure 6c) for σ_1 in Equation (6) to calculate the minimum principal stress, σ_3 , needed for fracturing in an extensional tectonic regime and plot it as a function of depth (Figure 8).

The Coulomb criterion for extensional tectonic regimes for all considered cases of intact basalt on Vesta predicts stresses that are entirely negative at all depths within the crust and mantle (Figure 8). As per our sign convention, negative stresses are tensile, which do not produce faults but instead form joints. This indicates that jointing would be the preferred fracturing mode for the entire brittle portion of the lithosphere consisting of intact basalt in an extensional tectonic regime on Vesta. The gravitational acceleration at any depth is too low to produce overburden pressures large enough to favor frictional sliding at any depth in the crust and mantle.

However, this result pertains to faulting of lithospheres with strength properties of intact rock. No rock mass on the scale of a lithosphere is, or ever was intact, and so the depth of jointing down to the lower mantle for intact rock properties is one extreme end-member case. Adjustment

of the Coulomb criterion for a basaltic rock mass that assumes a moderate to high degree of fracturing drastically reduces the appropriate value of unconfined compressive strength to as low as $\sigma_c = 10$ MPa (Schultz, 1995). The results of the adjusted calculation are also shown in Figure 8. The curve is shifted towards positive stresses, with stresses below ~14 km all being compressive. This indicates that even in a moderately to highly fractured lithosphere, jointing is the preferred fracturing mode in the upper ~14 km of the crust, with stresses favorable for frictional sliding, and thus normal faulting only below that. If a moderately to highly fractured lithosphere represents another endmember case, extensional tectonics in Vesta's lithosphere are dominated by opening-mode fractures in at least the upper 14 km. Only fractures much deeper than 14 km would be of sufficient size for the overburden to be large enough to allow for frictional sliding to form normal faults.

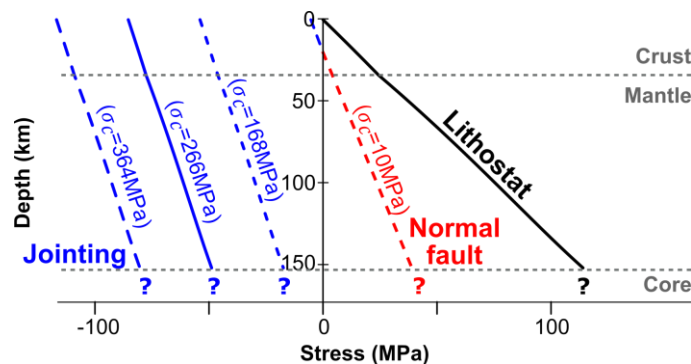


Figure 8. Solutions to the Coulomb criterion for a lithosphere under extension on Vesta. Solutions using rock properties of intact basalt ($\sigma_c = 168$ MPa, 233 MPa, and 364 MPa) and a moderately to highly fractured basaltic rock mass ($\sigma_c = 10$ MPa). Stresses that predict jointing are marked in blue and those predicting normal faults are indicated in red. <1 column, color>

5. Discussion

We investigated map patterns and the geomorphology of the large-scale troughs on Vesta, as well as the lithospheric fracturing behavior to assess possible fracturing behaviors that could have formed these troughs. Map patterns, geomorphology, and rock mechanical assessments individually and together have important implications for the tectonics on Vesta.

First, we observed that the rims of the troughs are scalloped (Figure 2a) and that these troughs mostly resemble V- and bowl-shaped cross-sectional geometries (Figure 3, supplementary materials). These observations are atypical for graben. In contrast to findings in previous studies (Buczowski et al., 2012; Schäfer et al., 2014; Scully et al., 2014; Yingst et al., 2014), a distinct flat-floor is not commonly observed on the vast majority of the troughs, but such flat floors are typically preserved over billions of years on terrestrial bodies, such as Moon (Lucchitta and Watkins, 1978), Mars (Kneissl et al., 2015; Ruj et al., 2019), or Mercury (Basilevsky et al., 2011; Klimczak et al., 2013). The rims of the troughs are too degraded to identify diagnostic fault traces of grabens. If the troughs were heavily degraded graben, their degraded geomorphology would be in stark contrast to the coeval Rheasilvia impact basin terracing scarps (e.g., Matronalia Rupes, labeled in Figure 1), which appear remarkably fresh. Suggested by previous geological evidence that the equatorial troughs formed related to the Rheasilvia impact basin (Jaumann et al., 2012), it would be unusual then that flat-floored grabens are heavily degraded but basin terracing scarps are well preserved. In contrast, joints naturally form steeply dipping V-shape opening, which can be degraded due to slope instability on the fracture walls and modified into wide bowl- or V-shapes by infilling of slope materials into the opening. This hypothesis better explains the degraded rims, coalesced pits, and the cross-sectional geometry and is compatible with the well-preserved impact basin terracing scarps.

Only one trough shows a direct transition to a pit crater chain, which narrows toward the tips and directly transitions into a pit crater chain, which then aligns with smaller pits further away from the end of the trough (Figure 2a). Another well-preserved pit chain was found to have larger pits in the middle and smaller pits at the two ends (Figure 2b). These patterns were also observed associated with grabens on Mars (Wyrick et al., 2004). There, pit crater chains have larger pits in the center of the chain and smaller pits at the ends representing different stages of formation (Wyrick et al., 2004). However, the martian pits are frequently found to be located on the floor of grabens (Wyrick et al., 2004), which we do not observe on Vesta. On the other hand, an opening-mode fracture origin may be an explanation of the absence of fault-bordered pits. Additionally, the pit craters are circular depressions that form by the collapse of material into subsurface voids, which may represent subsurface fractures that did not propagate to the surface. In this case, the preserved pit crater chain with larger pits in the center of the chain and smaller pits at the end (Figure 2b) is consistent with joints, in such that the maximum aperture is commonly found at the center of the length with smaller apertures near the tips (e.g., Vermilye and Scholz, 1995).

The relief and width of the troughs have implications for the graben and opening-mode fracture interpretation by relating them to the corresponding structural components. The trough reliefs were associated with the vertical displacements of graben components by the analysis from Buczkowski et al. (2012). We collected measurements of elevation differences between the trough floor and rims along the trough length and observed that the relief distributions do not show a general peak near the center and taper toward the tips of the troughs and that the maximum reliefs are located at different locations along the bounding scarps of every structure investigated (Figure 4). Following observations of the mechanics of fault growth (e.g., Dawers et al., 1993; Cartwright et al., 1996), our observations for the troughs would imply that the proposed graben-bounding

faults originated at different positions but then grew toward one another to interact and form grabens. However, none of the patterns of faulting interaction, such as segmentation and linkage are observed in the mapping. Such fault growth and mismatch in locations of maximum displacements are atypical for graben and therefore rule out a graben origin.

However, the width of troughs may serve as a measure for apertures of opening-mode fractures. We found that three out of four mapped equatorial troughs have their maximum width occurring at a similar position along the trough set (Figure 5) and the cumulative width distribution shows a roughly symmetric profile with one general maximum at the center of the overall length trace, tapering toward the tips. These are consistent with observations of opening-mode fracture mechanics, where the displacement distribution profiles display centrally located displacement maxima that taper to zero at the fracture tips for individual joints (e.g., Vermilye and Scholz, 1995). At the same time, the cumulative profile suggests that the troughs in the same set belong to one population, which formed under the same opening event, and thus the troughs may be part of a large set of parallel joints. Such opening-mode fracture patterns and aperture distributions are commonly observed on Earth, such as the parallel joints at Arches National Park, Utah (Cruikshank and Aydin, 1994), veins in the Culpeper Quarry, Virginia (Vermilye and Scholz, 1995) and the Ship Rock dikes in New Mexico (Delaney and Pollard, 1981), and on Mars, such as joints in west Candor Chasma and dikes in Coprates Chasma (Okubo, 2010).

Importantly, the calculated lithospheric strength shows that Vesta's crust and upper mantle are completely brittle for every combination of plausible parameters applicable to the asteroid. Based on that, the Coulomb criterion predicts the overburden pressure does not contribute significantly that in an extensional tectonic regime normal faulting at substantial depth is only possible when the stresses at the surface are tensile. The transition from opening to sliding-mode

fracturing is predicted by the Coulomb criterion to occur at a minimum of 14 km depth, but likely deeper, possibly down to the core-mantle boundary. Thus, normal faulting on Vesta is not required to explain the troughs, but even if any normal faulting occurred at depth, it should have been preceded or accompanied by large opening-mode fractures at the surface. Large openings triggered by normal faulting are also observed on Earth. One prominent analogue on Earth is the Almannagjá normal fault, forming the western boundary of the Þingvellir Graben at the Reykjaneshryggur-Langjökull rift system of southwest Iceland. The fault is accompanied by joints, or fissures, which opened up by up to 60 m before the fractures were large and deep enough for them to be reactivated as normal faults that then produced a vertical displacement of 40 m (Gudmundsson, 1992, 2011). Similar structures can also be found at other extensional tectonic settings on Earth, including the Kīlauea volcano rift zone in Hawaii (Holland et al., 2006) and the Ethiopian Rift in East Africa (Acocella et al., 2003).

A series of our geological observations are inconsistent with the graben interpretation but instead point to an opening-mode fracture origin for Vesta's large-scale troughs. We propose that the V-shaped and bowl-shaped troughs are likely to represent different stages of degrading and slumping of joints (Figure 9). Extension formed joints at both Vesta's surface and subsurface (Figure 9a). The slope material on the wall of the surface opening collapsed into the void, widening the initial sharp and narrow V-shape (n=31) and forming scalloped rims (Figure 9b). Collapse above subsurface openings formed pit crater chains (Figure 9b). Over time, slumping and degradation due to potential slope failure and impact shaking likely further widened the troughs and pit crater chains coalesced into linear troughs (Figure 9c). This process produced the observed flat-floored (n=53) and predominantly bowl-shaped trough geometries (n=176), regardless of whether the joint initially formed at the surface or subsurface, as shown in Figure 9a.

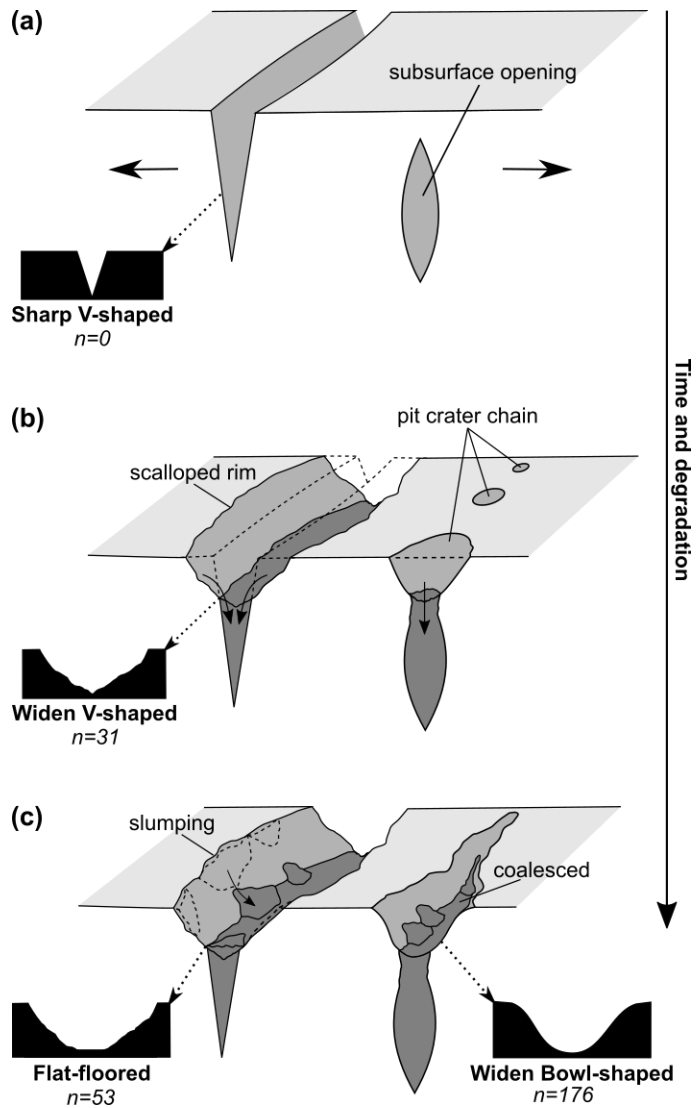


Figure 9. Diagram showing the geomorphologic evolution for opening-mode fractures on Vesta. (a) Large-scale jointing occurs on the surface and at the subsurface. (b) Steep joint walls immediately collapse into the void for the surface joint, forming a wide V-shape, whereas the collapse of subsurface opening forms a pit crater chain. (c) Slumping and degradation further widen troughs to form flat floors and bowl shapes in cross section and coalesced the pit crater chains to form continuous troughs. <1 column, black and white>

6. Conclusions

We investigated the fracture origin for the large-scale troughs on Vesta by analyzing their map patterns, cross-sectional geometries, and shape variations along the lengths of the structures. Our observations of scalloped rims that bound V- and bowl-shaped troughs, as well as the relief-length variations along the troughs, are inconsistent with grabens and are better explained by an opening-mode fracture origin. The measured individual and cumulative width-length variation and observations of pit crater chains are both consistent with those of opening-mode fracture populations. We therefore conclude that the troughs on Vesta represent large joints.

This conclusion is corroborated by our calculations of Vesta's lithospheric strength and fracturing behavior. Based on the end-member thermal models from Fu et al. (2014), the solutions of strength envelopes suggest that Vesta's lithosphere displays mostly a brittle behavior throughout its geologic history. Using the Coulomb criterion for the brittle lithosphere then predicts that even for highly fractured basaltic rock masses, frictional sliding and thus normal faulting can only take place at a depth below 14 km, and requires the formation of joints in the rock column above that depth. We, therefore, further conclude that the observed relief of the trough was not produced by faulting and should not be considered as vertical displacement.

In sum, we find multiple lines of geological evidence, including map patterns, trough geomorphologies, and considerations of fracture- and rock mechanics, that are, in most cases, inconsistent with the previously assumed fault origin of the troughs. Instead, observations overwhelmingly point to an opening-mode fracture origin of the troughs. Our findings and proposed evolution of large-scale joints are important for the understanding of the tectonic history of Vesta and may even help provide insight to identifying the type and formation of sizeable fractures on other small, low-gravity planetary bodies.

References

- Acocella, V., Korme, T., Salvini, F., 2003. Formation of normal faults along the axial zone of the Ethiopian Rift. *Journal of structural Geology* 25, 503-513.
- Basilevsky, A.T., Head, J.W., Fassett, C.I. and Michael, G., 2011. History of tectonic deformation in the interior plains of the Caloris basin, Mercury. *Solar System Research*, 45(6), pp.471-497.
- Bowling, T.J., Johnson, B.C., Melosh, H.J., Ivanov, B.A., O'Brien, D.P., Gaskell, R., Marchi, S., 2013. Antipodal terrains created by the Rheasilvia basin forming impact on asteroid 4 Vesta. *Journal of Geophysical Research: Planets* 118, 1821-1834.
- Buczowski, D.L., Wyrick, D.Y., Iyer, K.A., Kahn, E.G., Scully, J.E.C., Nathues, A., Gaskell, R.W., Roatsch, T., Preusker, F., Schenk, P.M., Corre, L.L., 2012. Large-scale troughs on Vesta: A signature of planetary tectonics. *Geophysical Research Letters* 39, L18205.
- Burov, E.B., Diament, M., 1992. Flexure of the continental lithosphere with multilayered rheology. *Geophysical Journal International* 109, 449-468.
- Byerlee, J.D., 1978. Friction of Rocks. *Pure and Applied Geophysics* 116, 615–626.
- Caristan, Y., 1982. The transition from high temperature creep to fracture in Maryland diabase. *Journal of Geophysical Research: Solid Earth* 87, 6781-6790.
- Cartwright, J.A., Mansfield, C., Trudgill, B., 1996. The growth of normal faults by segment linkage. *Geological Society, London, Special Publications* 99, 163-177.
- Crane, K.T., Klimczak, C., 2017. Timing and Rate of Global Contraction on Mercury. *Geophysical Research Letters* 44, 3082–3089.
- Cruikshank, K.M. and Aydin, A., 1994. Role of fracture localization in arch formation, Arches National Park, Utah. *Geological Society of America Bulletin*, 106(7), pp.879-891.

- Dawers, N.H., Anders, M.H. and Scholz, C.H., 1993. Growth of normal faults: Displacement-length scaling. *Geology*, 21(12), pp.1107-1110.
- Delaney, P.T., Pollard, D.D., 1981. Deformation of host rocks and flow of magma during growth of minette dikes and breccia-bearing intrusions near Ship Rock, New Mexico. USGPO.
- Ermakov, A.I., Zuber, M.T., Smith, D.E., Raymond, C.A., Balmino, G., Fu, R.R., Ivanov, B.A., 2014. Constraints on Vesta's interior structure using gravity and shape models from the Dawn mission. *Icarus* 240, 146-160.
- Fossen, H., 2009. Faults. *in* Structural Geology: Cambridge, UK, Cambridge University Press, 151-188.
- Fu, R.R., Hager, B.H., Ermakov, A.I., Zuber, M.T., 2014. Efficient early global relaxation of asteroid Vesta. *Icarus* 240, 133-145.
- Goetze, C., Evans, B., 1979. Stress and temperature in the bending lithosphere as constrained by experimental rock mechanics. *Geophysical Journal International* 59, 463-478.
- Gordon, R.G., 1998. The plate tectonic approximation: Plate nonrigidity, diffuse plate boundaries, and global plate reconstructions. *Annu. Rev. Earth Planet. Sci.* 26, 615–642.
- Gudmundsson, A., 1992. Formation and growth of normal faults at the divergent plate boundary in Iceland. *Terra Nova* 4, 464-471.
- Gudmundsson, A., 2011. Rock fractures in geological processes. Cambridge University Press.
- Hauber, E., Kronberg, P., 2005. The large Thaumasia graben on Mars: Is it a rift? *Journal of Geophysical Research: Planets* 110, E07003.
- Holland, M., Urai, J.L., S. Martel, S., 2006. The internal structure of fault zones in basaltic sequences. *Earth and Planetary Science Letters* 248, 301-315.

- Jaumann, R., Williams, D.A., Buczkowski, D.L., Yingst, R.A., Preusker, F., Hiesinger, H., Schmedemann, N., Kneissl, T., Vincent, J.B., Blewett, D.T., Buratti, B.J., 2012. Vesta's shape and morphology. *Science* 336, 687-690.
- Klimczak, C., Ernst, C. M., Byrne, P. K., Solomon, S. C., Watters, T. R., Murchie, S. L., Preusker, F., Balcerski, J. A., 2013. Insights into the subsurface structure of the Caloris basin, Mercury, from assessments of mechanical layering and changes in long-wavelength topography. *Journal of Geophysical Research (Planets)* 118, 2030–2044.
- Kneissl, T., Michael, G.G., Platz, T. and Walter, S.H.G., 2015. Age determination of linear surface features using the Buffered Crater Counting approach—Case studies of the Sirenum and Fortuna Fossae graben systems on Mars. *Icarus*, 250, pp.384-394.
- Lucchitta, B.K. and Watkins, J.A., 1978. Age of graben systems on the Moon. In *Lunar and Planetary Science Conference Proceedings (Vol. 9, pp. 3459-3472)*.
- Mackwell, S.J., Bai, Q., Kohlstedt, D.L., 1990. Rheology of olivine and the strength of the lithosphere. *Geophysical Research Letters* 17, 9-12.
- Okubo, C.H., 2010. Structural geology of Amazonian-aged layered sedimentary deposits in southwest Candor Chasma, Mars. *Icarus* 207, 210-225
- Okubo, C.H. and Martel, S.J., 1998. Pit crater formation on Kilauea volcano, Hawaii. *Journal of Volcanology and Geothermal Research*, 86(1-4), pp.1-18.
- Olson, J. E., Sublinear scaling of fracture aperture versus length: An exception or the rule?, *J. Geophys. Res.*, 108(B9), 2413, doi:10.1029/2001JB000419, 2003.
- Pfiffner, O.A., Ramsay, J.G., 1982. Constraints on geological strain rates: arguments from finite strain states of naturally deformed rocks. *Journal of Geophysical Research: Solid Earth* 87, 311-321.

- Pollard, D.D., Aydin, A., 1988. Progress in understanding jointing over the past century. Geological Society of America Bulletin 100, 1181-1204.
- Preusker, F., Scholten, F., Matz, K.-D., Roatsch, T., Jaumann, R., Raymond, C. A., & Russell, C. T. (2014). Global Shape of Vesta from Dawn FC stereo images. Paper presented at the 45th Lunar Planetary Science Conference, Lunar and Planetary Institute, Houston, TX.
- Ranalli, G., Murphy, D.C., 1987. Rheological stratification of the lithosphere. Tectonophysics 132, 281-295.
- Ruesch, O., Hiesinger, H., Blewett, D.T., Williams, D.A., Buczkowski, D., Scully, J., Yingst, R.A., Roatsch, T., Preusker, F., Jaumann, R., Russell, C.T., 2014. Geologic map of the northern hemisphere of Vesta based on Dawn Framing Camera (FC) images. Icarus 244, 41-59.
- Ruj, T., Komatsu, G., Pasckert, J.H. and Dohm, J.M., 2019. Timings of early crustal activity in southern highlands of Mars: Periods of crustal stretching and shortening. Geoscience Frontiers, 10(3), pp.1029-1037.
- Russell, C.T., Raymond, C.A., 2011. The Dawn mission to Vesta and Ceres. Springer New York, 3-23.
- Russell, C.T., Raymond, C.A., Coradini, A., McSween, H.Y., Zuber, M.T., Nathues, A., Sanctis, M.C.D., Jaumann, R., Konopliv, A.S., Preusker, F., S. W. Asmar, S.W., 2012. Dawn at Vesta: Testing the protoplanetary paradigm. Science 336, 684-686.
- Ruzicka, A., Snyder, G.A., Taylor, L.A., 1997. Vesta as the howardite, eucrite and diogenite parent body: Implications for the size of a core and for large-scale differentiation. Meteoritics & Planetary Science 32, 825-840.

- Schäfer, M., Nathues, A., Williams, D.A., Mittlefehldt, D.W., Corre, L.L., Buczkowski, D.L., Kneissl, T., Thangjam, G.S., Hoffmann, M., Schmedemann, N., Schäfer, T., 2014. Imprint of the Rheasilvia impact on Vesta—Geologic mapping of quadrangles Gegania and Lucaria. *Icarus* 244, 60-73.
- Schultz, R.A., 1995. Limits on strength and deformation properties of jointed basaltic rock masses. *Rock Mechanics and Rock Engineering* 28, 1-15.
- Schultz, R.A., 1997. Displacement-length scaling for terrestrial and Martian faults: Implications for Valles Marineris and shallow planetary grabens. *Journal of Geophysical Research: Solid Earth* 102, 12009-12015.
- Schultz, R.A., Moore, J.M., Grosfils, E.B., Tanaka, K.L., Mege, D., 2007. The Canyonlands model for planetary grabens: Revised physical basis and implications. *The Geology of Mars: Evidence from Earth-Based Analogs*: Cambridge, UK, Cambridge University Press, 371-399.
- Schultz, R.A., Okubo, C.H., Wilkins, S.J., 2006. Displacement-length scaling relations for faults on the terrestrial planets. *Journal of Structural Geology* 28, 2182-2193.
- Scully, J.E., Yin, A., Russell, C.T., Buczkowski, D.L., Williams, D.A., Blewett, D.T., Buesch, O., Hiesinger, H., Corre, L.L., Mercer, C., Yingst, R.A., 2014. Geomorphology and structural geology of Saturnalia Fossae and adjacent structures in the northern hemisphere of Vesta. *Icarus* 244.
- Sierks, H., Keller, H.U., Jaumann, R., Michalik, H., Behnke, T., Bubenhausen, F., Břttner, I., 2011. The Dawn Framing Camera. *Space science reviews* 163, 263-327.

- Sterenborg, M.G., Crowley, J.W., 2013. Thermal evolution of early solar system planetesimals and the possibility of sustained dynamos. *Physics of the Earth and Planetary Interiors* 214, 53-73.
- Stickle, A.M., Schultz, P.H., Crawford, D.A., 2015. Subsurface failure in spherical bodies: A formation scenario for linear troughs on Vesta's surface. *Icarus* 247.
- Vermilye, J.M., Scholz, C.H., 1995. Relation between vein length and aperture. *Journal of structural geology* 17, 423-434.
- Wyrick, D., Ferrill, D.A., Morris, A.P., Colton, S.L., Sims, D.W., 2004. Distribution, morphology, and origins of Martian pit crater chains. *Journal of Geophysical Research: Planets* 109.
- Yingst, R.A., Mest, S.C., Berman, D.C., Garry, W.B., Williams, D.A., Buczkowski, D., Jaumann, R., Pieters, C.M., Sanctis, M.C.D., Frigeri, A., Corre, L.L., 2014. Geologic mapping of Vesta. *Planetary and Space Science* 103, 2-23.
- Zuber, M.T., McSween, H.Y., Binzel, R.P., Elkins-Tanton, L.T., Konopliv, A.S., Pieters, C.M., Smith, D.E., 2011. Origin, internal structure and evolution of 4 Vesta. *Space science reviews* 163, 77-93.